


**Quantum oscillations and weak anisotropic resistivity in the chiral fermion semimetal PdGa**Xiang-Yu Zeng,<sup>\*</sup> Zheng-Yi Dai,<sup>\*</sup> Sheng Xu,<sup>\*</sup> Ning-Ning Zhao,<sup>\*</sup> Huan Wang, Xiao-Yan Wang, Jun-Fa Lin, Jing Gong, Xiao-Ping Ma, Kun Han, Yi-Ting Wang, Peng Cheng, Kai Liu,<sup>†</sup> and Tian-Long Xia<sup>‡</sup>*Department of Physics, Renmin University of China, Beijing 100872, People's Republic of China  
and Beijing Key Laboratory of Opto-electronic Functional Materials & Micro-nano Devices,  
Renmin University of China, Beijing 100872, People's Republic of China* (Received 9 March 2022; revised 26 August 2022; accepted 26 October 2022; published 10 November 2022)

We perform a detailed analysis of the magnetotransport and de Haas–van Alphen (dHvA) oscillations in crystal PdGa which is predicted to be a typical chiral fermion semimetal from the CoSi family holding a large Chern number. The unsaturated quadratic magnetoresistance and nonlinear Hall resistivity indicate that PdGa may be a multiband system with slight electron-hole compensation. Angular dependence of resistivity in PdGa shows weak anisotropy with twofold or threefold symmetry when the magnetic field rotates within the (1 $\bar{1}$ 0) or (111) plane perpendicular to the current. Nine or three frequencies are extracted after the fast Fourier-transform analysis of the dHvA oscillations with  $B \parallel [001]$  or  $B \parallel [011]$ , respectively, which is confirmed to be consistent with the Fermi surfaces obtained from first-principles calculations with spin-orbit coupling considered.

DOI: [10.1103/PhysRevB.106.205120](https://doi.org/10.1103/PhysRevB.106.205120)**I. INTRODUCTION**

The discovery of topological materials has kick started a revolution in the field of condensed-matter physics. Dirac and Weyl semimetals have been widely studied due to their novel properties [1,2], such as high mobility, low carrier concentration, large magnetoresistance (MR), chiral anomaly induced negative magnetoresistance (NMR), etc. In addition to the well-known inversion-symmetry-broken Weyl semimetal TaAs and its family members which hold spin-1/2 Weyl fermions [3], some new types of fermionic excitations have been proposed to possess large Chern numbers, namely, the spin-1 excitation [4–6], the double-Weyl fermion [5,7], and the spin-3/2 Rartia-Schwinger-Weyl (RSW) fermion [8–10], etc. Recently, lots of significant work on CoSi, RhSi, and RhSn has confirmed the existence of these predicated fermions [11–19], which brings a further deep understanding of the chiral fermions. These materials hold the spin-1 excitation at  $\Gamma$ , the double-Weyl fermion at  $R$  in the first Brillouin zone with Chern number  $\pm 2$ , and two Fermi arcs connect the Weyl points on the surface states without spin-orbit coupling (SOC). The band splitting might be obvious once the SOC is included. Furthermore, the spin-1 excitation and double-Weyl fermion evolve into a spin-3/2 RSW fermion and a time-reversal (TR) doubling of the spin-1 excitation with Chern number  $\pm 4$ , respectively. Meanwhile, the two Fermi arcs split, which is hardly observed in angle-resolved photoemission spectroscopy (ARPES) due to the weak SOC in CoSi and RhSi. Recently, ARPES and scanning tunneling microscopy results on PdGa have confirmed the existence of the pre-

dicted topological chiral surface Fermi arcs and band splitting due to the relatively stronger SOC [20,21]. Meanwhile, a detailed study on the magnetotransport properties in PdGa is lacking.

In this paper, we grew the high quality single crystals of PdGa, measured the transport properties, and studied its electronic structure through de Haas–van Alphen (dHvA) effect. Similar band structure and properties with its family materials CoSi [15] or PtGa [22] have been obtained whereas detailed differences on the Fermi-surface structure exist. PdGa holds spin-1 excitation at  $\Gamma$ , the double-Weyl fermion at  $R$  in the first Brillouin zone without SOC, carrying Chern number  $\pm 2$ . The band splits when SOC is considered, which makes the spin-1 excitation and double-Weyl fermions evolve into the spin-3/2 RSW fermion and the TR doubling of the spin-1 excitation with Chern number  $\pm 4$ , respectively [20]. The transverse magnetoresistance of PdGa shows unsaturated behavior, and the Hall conductivity can be described appropriately with the two-band model, which indicates that PdGa is a multiband system. The angular dependence of resistivity, an effective probe method for detecting the shape of the bulk Fermi surfaces (FSs), is employed to explore PdGa. The distinct dHvA oscillations have been observed, and nine fundamental frequencies have been extracted after the fast Fourier-transform (FFT) analysis when the magnetic field is applied along the [001] direction, which is consistent with the first-principles calculations when SOC is considered. The light cyclotron effective masses are extracted from the fitting of the thermal factor in the Lifshitz-Kosevich (LK) formula, indicating the possible existence of massless quasiparticles.

**II. EXPERIMENTAL AND CRYSTAL STRUCTURE**

The single crystals of PdGa were grown from bismuth flux. The starting elements, palladium powder, gallium ingot, and

<sup>\*</sup>These authors contributed equally to this paper.

<sup>†</sup>kliu@ruc.edu.cn

<sup>‡</sup>tlxia@ruc.edu.cn

excess bismuth granules were put into the corundum crucible and sealed in a quartz tube with a ratio of Pd: Ga: Bi = 1:1:20. The quartz tube was heated to 950 °C at 60 °C/h and held for 20 h, then cooled to 400 °C at a rate of 1 °C/h at which the excess Bi flux was separated from the crystals by centrifugation. The obtained crystals have triangular or rectangular shapes with its size as large as 1–3 mm in one dimension. The atomic proportion of PdGa was checked to be Pd:Ga = 1:1 using energy dispersive x-ray spectroscopy (Oxford X-Max 50). The single crystal and powder x-ray diffraction (XRD) were collected from a Bruker D8 Advance x-ray diffractometer using Cu  $K\alpha$  radiation. TOPAS-4.2 was employed for the refinement. The resistivity and Hall measurements were performed on a Quantum Design physical property measurement system (QD PPMS-14T) using the standard six-probe method on a long flake crystal. The magnetization was measured with the vibrating sample magnetometer option of PPMS.

The first-principles electronic structure calculations on PdGa were performed by using the projector augmented-wave method [23,24] as implemented in the VASP package [25–27]. The generalized gradient approximation of the Perdew-Burke-Ernzerhof type [28] was used for the exchange-correlation functional. The kinetic-energy cutoff of the plane-wave basis was set to 370 eV. The Brillouin zone was sampled with a  $11 \times 11 \times 11$   $k$ -point mesh. For the Fermi surface broadening, the Gaussian smearing method with a width of 0.05 eV was adopted. The lattice constants and the atomic positions were fully relaxed until the forces on all atoms were smaller than 0.01 eV/Å. The relaxed lattice constants  $a = b = c = 4.953(0)$  Å are consistent with the experimental results. The spin-orbit coupling effect was included in the band structure calculations. The Fermi-surface planes were calculated based on the tight-binding Hamiltonian constructed with the maximally localized Wannier functions [29,30] for the outmost  $s$ ,  $p$ , and  $d$  orbitals of the Pd atom,  $s$ ,  $p$ , and  $d$  orbitals of the Ga atom generated by the first-principles calculations.

The crystal structure of PdGa is shown in Fig. 1(a), which crystallizes in a simple cubic structure with the  $P2_13$  (No. 198) space group. Figures 1(b) and 1(c) display the single-crystal XRD patterns with (111) and (001) reflections. The insets of Figs. 1(b) and 1(c) exhibit pictures of the typical grown PdGa crystals with the (111) and (001) crystal faces, respectively. The powder XRD pattern is shown in Fig. 1(d), which can be indexed to the structure of PdGa with the refined lattice parameter  $a = b = c = 4.89(0)$  Å.

### III. RESULTS AND DISCUSSIONS

The temperature dependence of resistivity is displayed in Fig. 2(a), which exhibits a metallic behavior fitted well below 75 K using the equation  $\rho_{xx}(T) = \rho_0 + AT^2$ , following a conventional Fermi-liquid behavior with the residual resistivity  $\rho_0 = 0.594 \mu\Omega \text{ cm}$  and  $A = 0.0005 \mu\Omega \text{ cm K}^{-2}$ . The relatively large residual resistivity ratio =  $\rho(300 \text{ K})/\rho(2 \text{ K}) \approx 37$  indicates the high quality of the grown crystals. As shown in the band structure, complex bands near the Fermi level contribute to the conductivity in PdGa, resulting in the metallic behavior different from that of a semimetal. Figure 2(b) presents the  $\text{MR} = [\rho_{xy}(B) - \rho_{xy}(0)]/\rho_{xy}(0)$  curves with  $B \parallel$

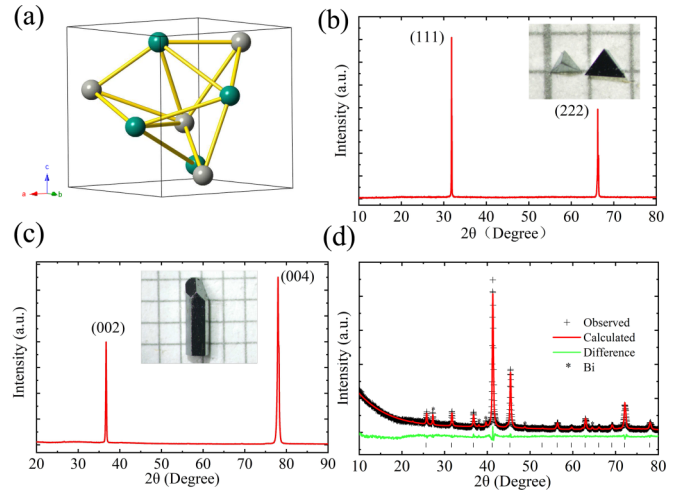


FIG. 1. (a) Crystal structure of PdGa. (b) and (c) Single-crystal XRD pattern of PdGa with (111) and (001). The insets show the picture of the grown crystal. (d) Powder XRD patterns and the Rietveld refinement of PdGa.

[111] at various temperatures, which reaches about 600% at 2.5 K and 14 T. As is shown, no sign of Shubnikov–de Haas oscillations was observed even the magnetic field is as large as 14 T. The field dependence of MR at 2.5 K with the magnetic field tilted from  $B \perp I$  ( $\theta = 0^\circ$ ) to  $B \parallel I$  ( $\theta = 90^\circ$ ) is exhibited in Fig. 2(c). The inset shows the definition of  $\theta$  which is the angle between the magnetic field and the current direction. The amplitude of MR decreases gradually with  $\theta$  and reaches a minimum when  $B \parallel I$  where the NMR has not been observed due to the orbital MR induced by the trivial holelike pockets at  $M$  or around the  $\Gamma$  point. In order

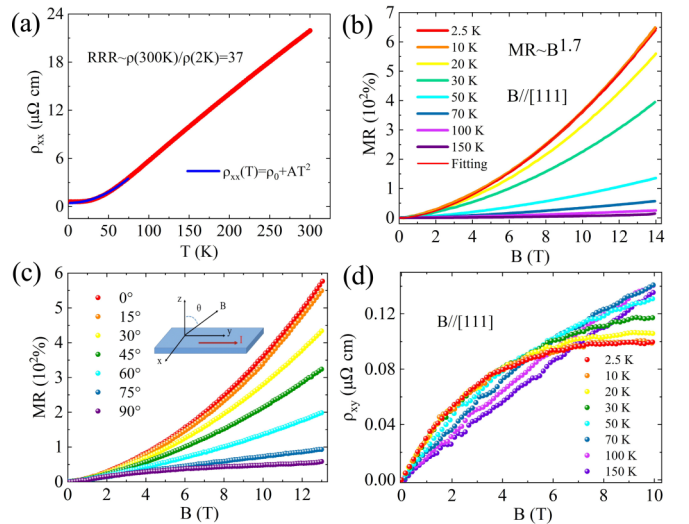


FIG. 2. (a) Temperature dependence of the resistivity  $\rho_{xx}$ . (b) Magnetic-field dependence of MR at different temperatures. The red line shows the fitting curve of MR at  $T = 2.5$  K with the formula  $\text{MR} \sim B^{1.7}$ . (c) Magnetic-field dependence of MR at 2.5 K with the magnetic field tilted from  $B \perp I$  ( $\theta = 0^\circ$ ) to  $B \parallel I$  ( $\theta = 90^\circ$ ). The inset shows the definition of  $\theta$ . (d) Magnetic-field dependence of Hall resistivity at various temperatures.

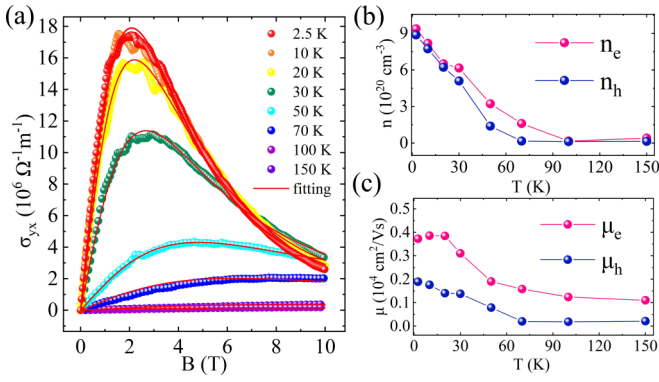


FIG. 3. (a) Field dependence of the Hall conductivity [ $\sigma_{yx} = \rho_{xy} / [(\rho_{xy})^2 + (\rho_{xx})^2]$ ] at various temperatures. (b) and (c) are the temperature dependence of carrier densities and mobility of the electrons and holes extracted from the two-band model fitting.

to demonstrate the characteristics of carriers in PdGa, we examine the evolution of the Hall resistivity  $\rho_{xy}$  at various temperatures from 2.5 to 150 K as shown in Fig. 2(d). The Hall resistivity reveals a nonlinear behavior especially when the temperature decreases, indicating that PdGa is a multiband system. Therefore, it is reasonable to fit the Hall conductivity with the two-band model,

$$\Delta\sigma_{yx} = \left( \frac{n_e \mu_e^2}{1 + (\mu_e B)^2} - \frac{n_h \mu_h^2}{1 + (\mu_h B)^2} \right) eB. \quad (1)$$

$n_{e,h}$  and  $\mu_{e,h}$  represent the concentration and mobility of electrons or holes, respectively. Figure 3(a) displays the field

dependence of Hall conductivity. The different color dots represent the experimental data whereas the red lines are fitting curves from which the temperature dependence of concentrations and mobilities are extracted as shown in Figs. 3(b) and 3(c). As the temperature decreases, both the concentration and the mobility of the two types of carriers increase. At 2.5 K,  $n_h = 8.8 \times 10^{20}$ ,  $n_e = 9.4 \times 10^{20} \text{cm}^{-3}$ , and  $\mu_h = 1890 \text{cm}^2$ , and  $\mu_e = 3700 \text{cm}^2 \text{V}^{-1} \text{s}^{-1}$ , respectively. The ratio of  $n_h/n_e = 0.936$  is close to 1, which indicates the possibility of the electron-hole compensation in PdGa. According to the semiclassical transport theory based on the Boltzmann equation, Kohler's rule is applicable if there is a single species of charge carrier, therefore, sometimes employed as a method to examine the existence of carrier compensation [31]. However,  $\text{MR} \sim B^{1.7}$  deviates from the quadratic behavior as shown in Fig. 2(b), indicating the violation of Kohler's rule. In fact, nonlinear behavior of Hall resistivity reveals that PdGa is a multiband system. There is more than one type of carrier and their mobilities have different temperatures and field dependences so will the magnetoresistance, making the violation of Kohler's rule possible.

The anisotropy in the resistivity at different fields is presented in Fig. 4. A naturally grown regular tetrahedron sample with the (111) plane is polished into a rectangular flake. Figure 4(a) shows the schematic of the field rotation where the current is applied along the  $[\bar{1}10]$  direction, and the magnetic field is rotated within the  $(\bar{1}10)$  plane. At 2.5 K, the  $\rho_{xx}$  at various fields are measured as presented in Fig. 4(b), which shows a weak twofold symmetry that becomes more evident as the field increases. It should be noted that there exist a few

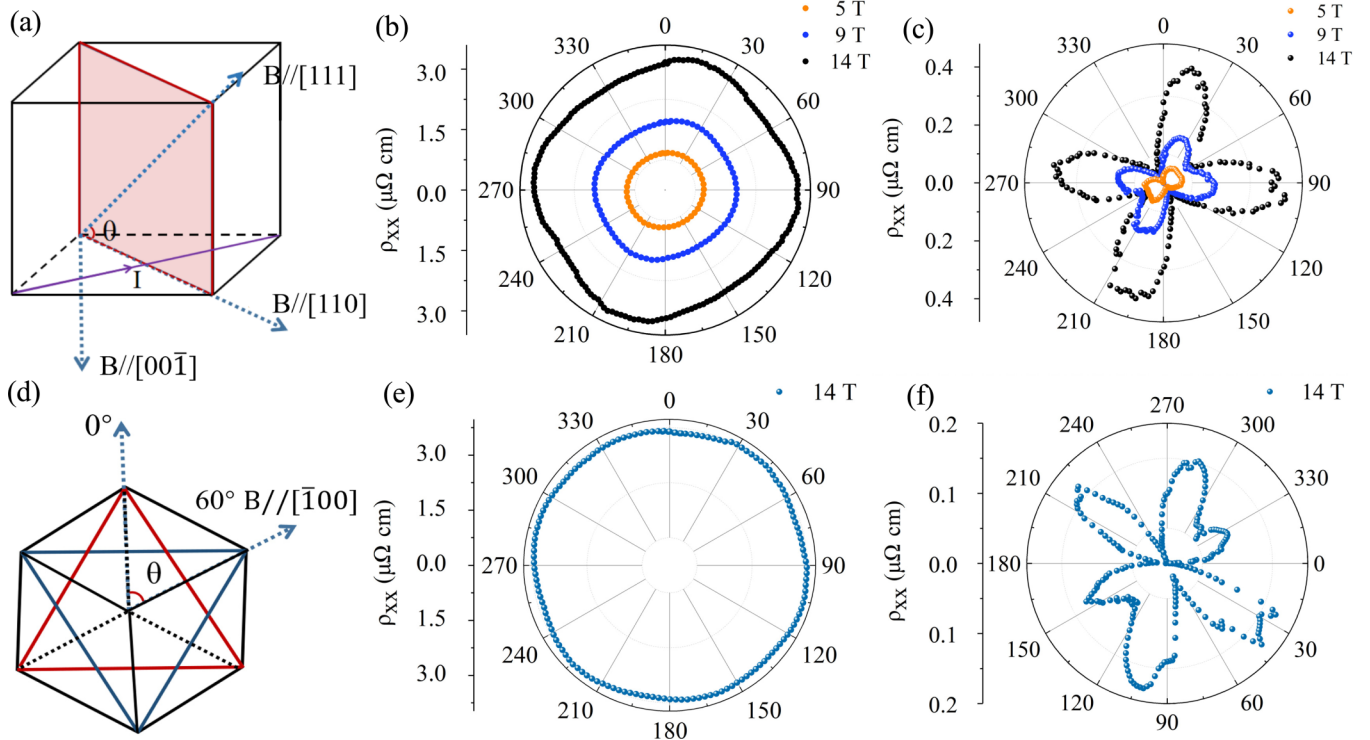


FIG. 4. (a) and (d) show the schematics of angular rotation. (b) Polar plot of  $\rho_{xx}$  under 5 T (yellow dots), 9 T (blue dots), and 14 T (black dots) with  $B$  vertical to  $I$  at 2.5 K. (c) Polar plot obtained from (b) after subtracting a minimum. (e) Polar plot of  $\rho_{xx}$  under 14 T with  $B$  vertical to  $I$  at 2.5 K. (f) Polar plot obtained from (e) after subtracting a minimum.

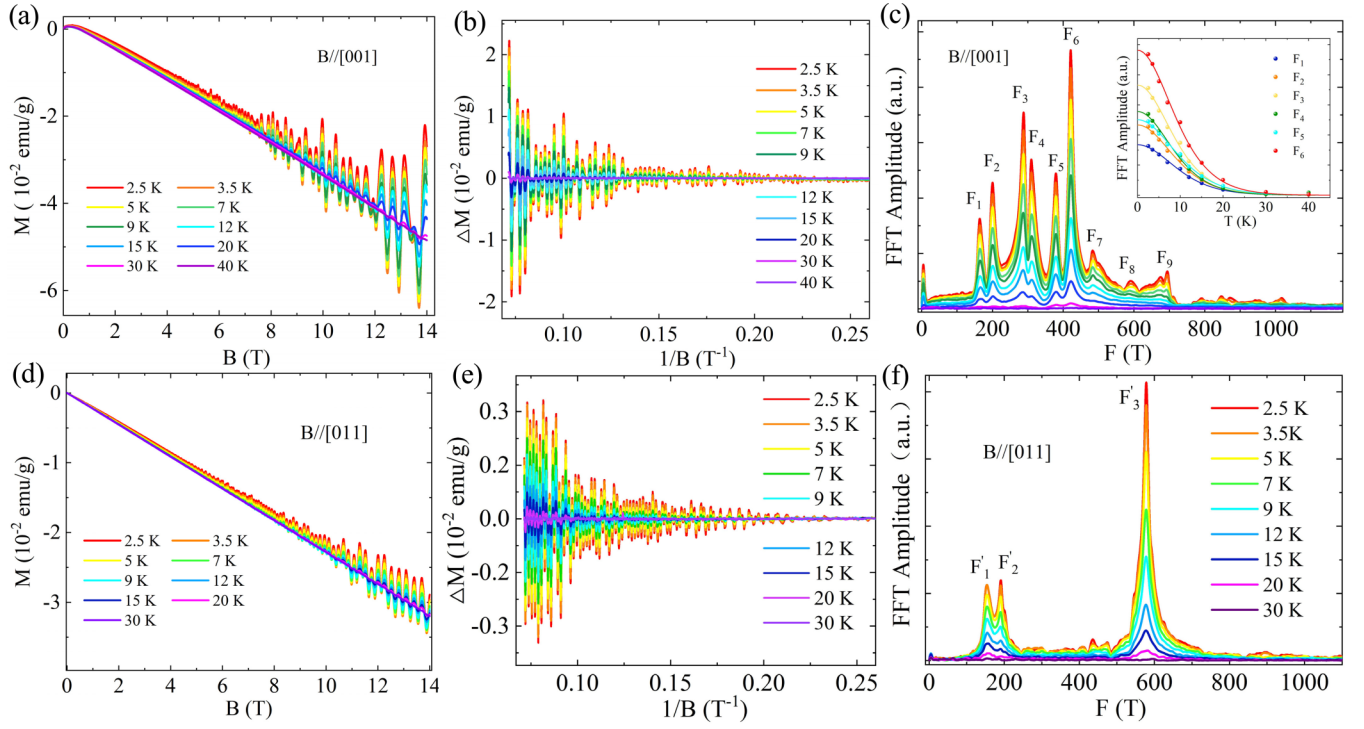


FIG. 5. (a) and (d) are the dHVA oscillations at various temperatures with the  $B \parallel [001]$  and  $B \parallel [011]$  configurations, respectively. (b) and (e) are the amplitudes of dHVA oscillations as a function of  $1/B$ . (c) and (f) are the FFT spectra of the oscillations extracted from (b) and (e), respectively. The inset of (c) is the temperature dependence of relative normalized FFT amplitude of the frequencies.

data points overlapping at the beginning and the end of the rotation which are not exactly the same especially when a higher field is applied. As shown in Fig. 4(c), the field dependence of resistivity is normalized by subtracting the minimal value of the oscillating resistivity at the corresponding field in the polar plot to enhance the feature of the slight anisotropy. An analogous experiment is conducted on another sample with  $B$  rotating within the (111) plane as shown in Fig. 4(d). A cuboid with a cross section of  $0.2 \times 0.2$  mm<sup>2</sup> was obtained after a regular tetrahedron sample was polished, and the current was applied along the direction of [111] (length of the sample) with the field rotating perpendicular to the current. Figure 4(e) shows a polar plot of  $\rho_{xx}$  at 14 T, which illustrates almost a circular shape. After subtracting a minimum from the raw data, six peaks with diverse intensities appear as exhibited in Fig. 4(f). These peaks can be divided into two groups with threefold symmetry, respectively, corresponding to the schematic of Fig. 4(d). Regarding the symmetry, a classical theory describes [32,33] that  $\rho(B)$  is dominated by the orbital effects deriving from the cyclotron motion of the electrons caused by Lorentz force, corresponding to the formula [34],

$$\text{MR} = \frac{\rho(B) - \rho(0)}{\rho(0)} \sim (w_c \tau)^2 \sim (e\tau/m^*)^2 B^2 \sim \mu^2 B^2, \quad (2)$$

where  $w_c$  is the cyclotron frequency,  $\tau$  is the scattering time,  $m^*$  is the effective mass, and  $B$  is the magnetic field. Although the relaxation time varies along different directions, in the simplest model, the difference is so small that we can

assume that  $\tau$  is a constant. Therefore, the anisotropy of the effective masses of carriers strongly affect the values of the angular dependence of resistivity, which is directly related to the shape of the FSs. Different from the previous study on bismuth [32,33] where valley polarization is induced at the high field and low temperature, resulting in symmetry breaking and anisotropic resistivity. The anisotropy in PdGa is relatively weak, the subtle difference of  $\tau$  or a small misalignment between the magnetic field rotation plane and the current direction may both cause significant asymmetry in the resistivity so that the symmetry is broken. The nonnegligible anisotropy of PdGa reveals the three-dimensional feature of the Fermi surface and the differences of the carrier mobility and effective masses for fields along different directions.

Previous ARPES results present the band splitting of surface states with different chiralities, signifying the existence of SOC in PdGa. On the other hand, quantum oscillation, usually an effective method to map the characteristics of FSs, is employed in this paper to study the electronic structure and SOC effect according to the Onsager relation  $F = (\phi_0/2\pi^2)A_F = (\hbar/2\pi e)A_F$ . The frequency  $F$  is proportional to the extreme cross-section ( $A_F$ ) of the FS normal to the magnetic field. As the field increases, the quantized Landau levels cross the Fermi energy ( $E_F$ ) successively, lead to the oscillation of the density of state at  $E_F$ , and eventually result in quantum oscillation in physical properties revealed by magnetic torque, magnetization, resistivity, thermopower, or thermal conductivity, etc. Figures 5(a) and 5(d) present the isothermal magnetization of a prismatic crystal as shown

TABLE I. Parameters derived from dHvA oscillations with  $B \parallel [001]$ .  $F_{\text{exp}}$  and  $F_{\text{cal}}$ , experimental and calculative oscillation frequency;  $m^*$ , effective mass;  $A_F$ , cross-sectional area of FS normal to the field.

	$F_1$	$F_2$	$F_3$	$F_4$	$F_5$	$F_6$	$F_7$	$F_8$	$F_9$
$F_{\text{exp}}$ (T)	164.0	200.4	288.1	310.7	378.8	421.7	483.8	590.4	693.9
$m^*/m_e$	0.081	0.085	0.089	0.088	0.079	0.084	0.076	0.077	0.092
$A_F(10^{-3} \text{ \AA}^{-2})$	15.63	19.12	27.50	29.66	36.15	40.26	46.18	56.35	66.23
$F_{\text{cal}}$ (T)	184.4	227.4	291.6	334.8	382.4	415.1	478.5	553.3	653.1

in the inset of Fig. 1(c) with  $B \parallel [001]$  and  $B \parallel [011]$  configurations, respectively, which both exhibit evident dHvA oscillations. The oscillatory components of magnetization are obtained after subtracting a smooth background as exhibited in Figs. 5(b) and 5(e). After the FFT analysis, nine/three fundamental frequencies are extracted as shown in Figs. 5(c) and 5(f). Thus, according to the Onsager relation, the corresponding extreme cross-section area of  $F_1$ - $F_9$  and  $F'_1$ - $F'_3$  with  $B \parallel [001]$  and  $B \parallel [011]$  are determined (see Tables I and II for details). The low frequency at about 3 T in the FFT spectra comes from the data processing instead of the intrinsic dHvA oscillations. The oscillatory component versus  $1/B$  is described by the LK formula,

$$\Delta M \propto -B^{1/2} \frac{\lambda T}{\sinh(\lambda T)} e^{-\lambda T_D} \sin \left[ 2\pi \left( \frac{F}{B} - \frac{1}{2} + \beta + \delta \right) \right], \quad (3)$$

where  $\lambda = (2\pi^2 k_B m^*)/(\hbar e B)$ .  $2\pi\beta$  is the Berry phase, and  $T_D$  is the Dingle temperature.  $\delta$  is a phase shift.  $\delta = 0$  and  $\pm 1/8$  for two-dimensional and three-dimensional systems, respectively. The thermal factor  $R_T = (\lambda T)/\sinh(\lambda T)$  in the LK formula has been employed to describe the temperature dependence of the FFT amplitude. As shown in the inset of Fig. 5(c), the temperature dependence of the relative FFT amplitude can be well fitted, and the extracted small effective masses are listed in Table I, presenting the characteristic of the Weyl fermion. Since the previous work has verified that PdGa is a topological semimetal with new types of fermions [20], the Berry phase from quantum oscillations is not presented here. In fact, Berry phases are extracted by the Landau-level index fan diagram whereas Landau indices  $n$  are so large that an inevitable error in the fitting is introduced. Thus, we made no further analysis to reprove the topological characteristics of PdGa.

The calculated band structure and FSs of PdGa with SOC in the Brillouin zone are displayed in Figs. 6(a) and 6(b). According to the first-principles calculations, the  $\Gamma$  and  $R$  points hold electronlike FSs with Chern number  $C = \pm 4$  whereas the

rest hold holelike FSs. In order to get a complete picture of the Fermi surface, detailed cross sections with different values of  $k_z$  in the direction of [001] were calculated. Figures 6(c)–6(e) exhibit ten extreme cross sections with  $B \parallel [001]$  in different  $k_z$  planes.  $S_1$  and  $S_2$  are extreme cross sections of two small drop-shaped pockets along  $\Gamma$ - $R$  cutting at  $k_z = 0.16\pi$ . Cross sections  $S_3$ – $S_6$  are projections of the FSs around the  $\Gamma$  point and  $S_7$ – $S_{10}$  show a quarter of FS's extreme cross sections at the  $M$  point on the  $k_z = 0$  plane. The calculated FSs on the (011) plane are exhibited in Fig. 6(f). According to the Onsager relation, when  $B \parallel [001]$ , the corresponding oscillation frequencies of  $S_1$ – $S_6$  are 184.4, 227.4, 291.6, 334.8, 382.4, and 415.1 T, which corresponds to the frequencies  $F_1$ – $F_6$  as shown in Table I, respectively. At  $k_z = 0.2\pi$ , there is a square extreme cross section in the center of the plane with calculated frequency about 478.5 T, corresponding to the frequency  $F_7$  (483.8 T). The calculated frequency of  $S'_7$  ( $4 \times S_7$ ) is 553.3 T, which is comparable to the obtained frequency  $F_8$  (590.4 T). In a strong magnetic field, carriers can be exchanged between two orbits through a small gap, which is called magnetic breakdown [35]. A touch of  $S_8$  and  $S_9$  along  $M$ - $X$  is quite apparent, which enables the carriers to move between two orbits in a strong field. Therefore, the corresponding frequency of the difference between  $S'_8$  ( $4 \times S_8$ ),  $S'_9$  ( $4 \times S_9$ ) is 653.1 T in accord with the observed frequency  $F_9$  (693.9 T).

In order to experimentally confirm the calculated FS structure from the calculations, the angular dependence of dHvA oscillations have been measured as displayed in Fig. 7. The schematic in Fig. 7(a) presents the rotation of the magnetic field where  $\theta$  is the angle between the magnetic field and [001] direction. We selected seven distinct angles between [001] and [011] for measurement with the field always within the (001) plane. As shown in Figs. 6(c) and 6(f), there are two drop-shaped extreme cross sections near the  $\Gamma$  point with  $B \parallel [001]$  and  $B \parallel [011]$ . It shows a good agreement with the results of the angular dependence of dHvA oscillations that  $F_1$  and  $F_2$  gradually split into four peaks as the magnetic-field  $B$  rotates from [001] to [011], which implies that two FSs evolve into four with different sizes, respectively. And frequencies  $F_3$  and  $F_4$  fade away at  $37.5^\circ$ , which exhibits the feature of the bone-shaped FSs as shown in Figs. 6(b). Two square-shaped extreme cross sections at the  $\Gamma$  point with  $B \parallel [001]$  becomes rectangular  $\sqrt{2}$  times larger when  $\theta = 45^\circ$  as shown in Figs. 6(d) and 6(f), which corresponds to the experimental results that  $F_5$  and  $F_6$  increase as  $\theta$  increases. Similar with the evolutionary trend of the  $F_2$  and  $F_3$ ,  $F_7$  gradually increases and disappears when  $\theta = 30^\circ$ , which is in accord with the feature of the endocyclic FS. A larger peak  $F_8$  decreases slightly when  $B$  turns to the [011] direction, which coincides with the

 TABLE II. Parameters derived from dHvA oscillations with  $B \parallel [011]$ .  $F_{\text{exp}}$  and  $F_{\text{cal}}$ , experimental and calculative oscillation frequencies;  $A_F$ , cross-sectional area of FS normal to the field.

	$F'_1$	$F'_2$	$F'_3$
$F_{\text{exp}}$ (T)	154.1	190.7	578.4
$A_F(10^{-3} \text{ \AA}^{-2})$	14.70	18.19	55.19
$F_{\text{cal}}$ (T)	178.1	222.6	546.2

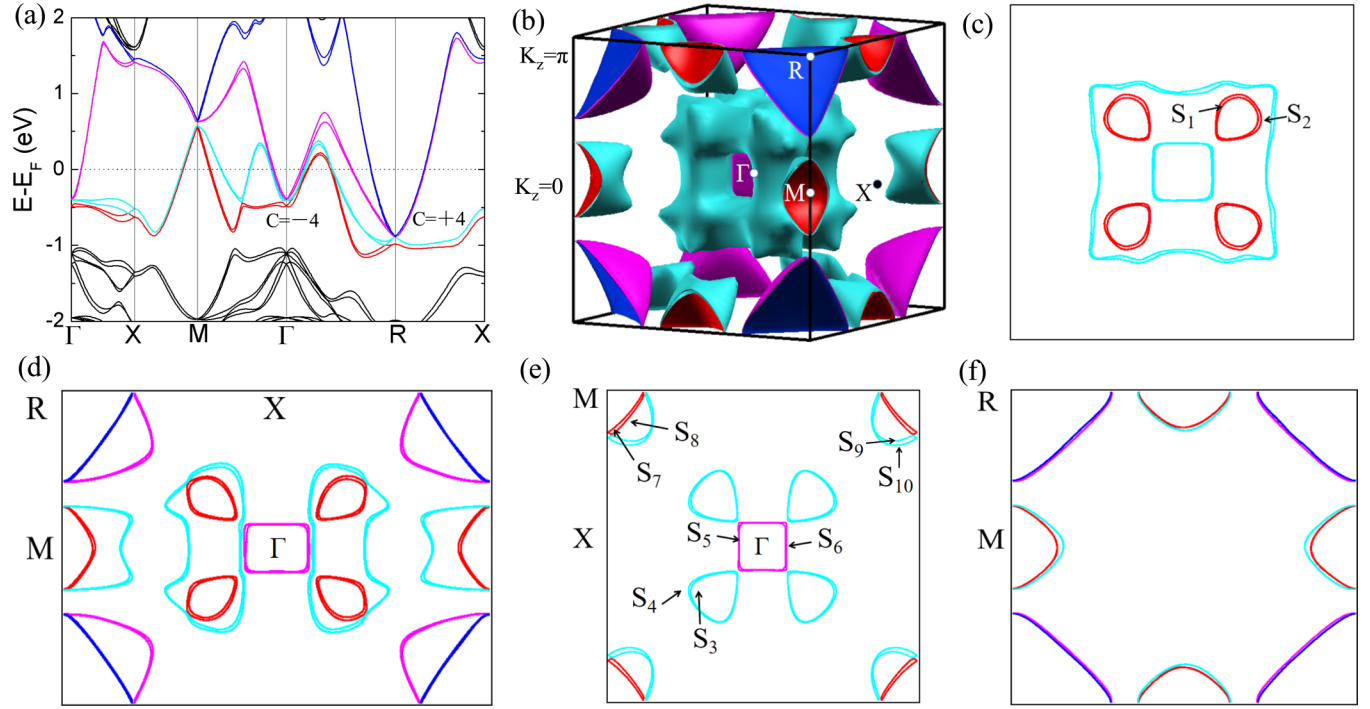


FIG. 6. (a) Calculated band structure of PdGa with SOC. (b) Calculated FSs in the Brillouin zone. (c), (d), (e), and (f) Calculated FSs on the  $k_z = 0.16\pi$  plane, the  $\Gamma$ -X-M-R plane, the  $k_z = 0$  plane, and the  $k_z = \pi$  plane, respectively.

extreme cross sections at the  $M$  point as shown in Figs. 6(d) and 6(f). As discussed above, magnetic breakdown occurs between two touched FSs of  $S_8$  and  $S_9$  with  $B \parallel [001]$ , so it is easily to be destroyed as the magnetic field deflects a little bit from  $[001]$ , corresponding to the change in  $F_9$  which is soon disappeared as  $\theta$  exceeds  $7.5^\circ$ . Thus, we confirm that the frequencies  $F_1, F_2, F_3, F_4$ , and  $F_7$  stem from the FSs along  $\Gamma$ -R

and  $\Gamma$ -M, whereas the frequencies  $F_5, F_6, F_8$ , and  $F_9$  originate from the FSs at the  $\Gamma$  and  $M$  points.

#### IV. SUMMARY

To summarize, the high quality single crystals of PdGa with the Bi flux are synthesized, which show metallic behaviors. The large unsaturated MR and Hall resistivities indicate that PdGa should be considered as a multiband system. Angular dependence of the resistivity study reveals weak anisotropy of twofold symmetry or threefold symmetry with  $B$  rotating on the (011) or (111) plane, respectively, corresponding to the symmetry of the FSs. Band splitting due to SOC in PdGa has been observed in quantum oscillations, which is consistent with the band structure and FSs obtained from first-principles calculations. The frequencies extracted from dHvA oscillations are well consistent with the FSs' extreme cross sections of first-principles calculations.

#### ACKNOWLEDGMENTS

This work was supported by the National Key R&D Program of China (Grant No. 2019YFA0308602), the National Natural Science Foundation of China (Grants No. 12074425 and No. 11874422), and the Research Funds of Renmin University of China (Grant No. 19XNLG18). K.L. was supported by the National Key R&D Program of China (Grant No. 2017YFA0302903), and the National Natural Science Foundation of China (Grant No. 11774424). Computational resources were provided by the Physical Laboratory of High Performance Computing at Renmin University of China.

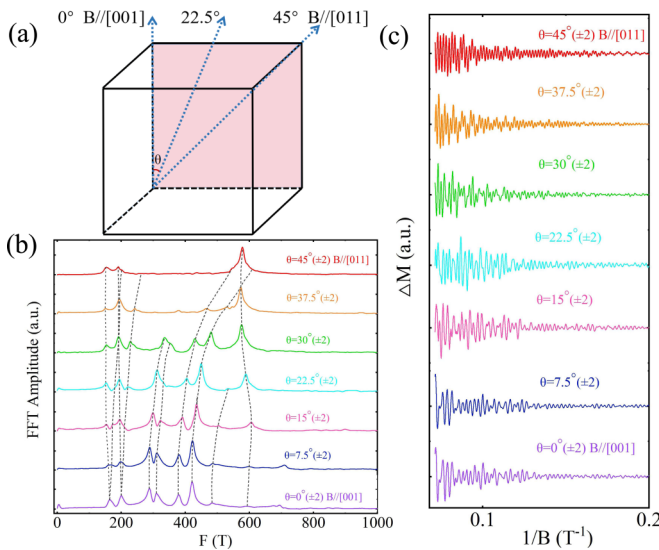


FIG. 7. (a) The sketch map of the respective rotating  $B$  direction along crystallographic direction. (b) Angular dependence of dHvA oscillations at 2.5 K. (c) Corresponding FFT spectra for  $B$  rotating from  $B \parallel [001]$  to  $B \parallel [011]$ .

- [1] T. Wehling, A. M. Black-Schaffer, and A. V. Balatsky, *Adv. Phys.* **63**, 1 (2014).
- [2] B. Yan and C. Felser, *Annu. Rev. Condens. Matter Phys.* **8**, 337 (2017).
- [3] H. Weng, C. Fang, Z. Fang, B. A. Bernevig, and X. Dai, *Phys. Rev. X* **5**, 011029 (2015).
- [4] J. L. Manes, *Phys. Rev. B* **85**, 155118 (2012).
- [5] P. Tang, Q. Zhou, and S.-C. Zhang, *Phys. Rev. Lett.* **119**, 206402 (2017).
- [6] B. Bradlyn, J. Cano, Z. Wang, M. Vergniory, C. Felser, R. J. Cava, and B. A. Bernevig, *Science* **353**, aaf5037 (2016).
- [7] Y. Xu and L.-M. Duan, *Phys. Rev. A* **94**, 053619 (2016).
- [8] L. Liang and Y. Yu, *Phys. Rev. B* **93**, 045113 (2016).
- [9] M. Ezawa, *Phys. Rev. B* **94**, 195205 (2016).
- [10] W. Rarita and J. Schwinger, *Phys. Rev.* **60**, 61 (1941).
- [11] D. Pshenay-Severin, Y. V. Ivanov, A. Burkov, and A. Burkov, *J. Phys.: Condens. Matter* **30**, 135501 (2018).
- [12] D. S. Sanchez, I. Belopolski, T. A. Cochran, X. Xu, J.-X. Yin, G. Chang, W. Xie, K. Manna, V. Süß, C.-Y. Huang *et al.*, *Nature (London)* **567**, 500 (2019).
- [13] Z. Rao, H. Li, T. Zhang, S. Tian, C. Li, B. Fu, C. Tang, L. Wang, Z. Li, W. Fan *et al.*, *Nature (London)* **567**, 496 (2019).
- [14] D. Takane, Z. Wang, S. Souma, K. Nakayama, T. Nakamura, H. Oinuma, Y. Nakata, H. Iwasawa, C. Cacho, T. Kim *et al.*, *Phys. Rev. Lett.* **122**, 076402 (2019).
- [15] X. Xu, X. Wang, T. A. Cochran, D. S. Sanchez, G. Chang, I. Belopolski, G. Wang, Y. Liu, H.-J. Tien, X. Gui *et al.*, *Phys. Rev. B* **100**, 045104 (2019).
- [16] D. Wu, Z. Mi, Y. Li, W. Wu, P. Li, Y. Song, G. Liu, G. Li, and J. Luo, *Chin. Phys. Lett.* **36**, 077102 (2019).
- [17] G. Chang, S.-Y. Xu, B. J. Wieder, D. S. Sanchez, S.-M. Huang, I. Belopolski, T.-R. Chang, S. Zhang, A. Bansil, H. Lin *et al.*, *Phys. Rev. Lett.* **119**, 206401 (2017).
- [18] S. Xu, L. Zhou, H. Wang, X.-Y. Wang, Y. Su, P. Cheng, H. Weng, and T.-L. Xia, *Phys. Rev. B* **100**, 245146 (2019).
- [19] H. Wang, S. Xu, X.-Q. Lu, X.-Y. Wang, X.-Y. Zeng, J.-F. Lin, K. Liu, Z.-Y. Lu, and T.-L. Xia, *Phys. Rev. B* **102**, 115129 (2020).
- [20] N. B. Schröter, S. Stolz, K. Manna, F. De Juan, M. G. Vergniory, J. A. Krieger, D. Pei, T. Schmitt, P. Dudin, T. K. Kim *et al.*, *Science* **369**, 179 (2020).
- [21] P. Sessi, F.-R. Fan, F. Küster, K. Manna, N. B. Schröter, J.-R. Ji, S. Stolz, J. A. Krieger, D. Pei, T. K. Kim *et al.*, *Nat. Commun.* **11**, 3507 (2020).
- [22] S. Xu, L. Zhou, X.-Y. Wang, H. Wang, J.-F. Lin, X.-Y. Zeng, P. Cheng, H. Weng, and T.-L. Xia, *Chin. Phys. Lett.* **37**, 107504 (2020).
- [23] P. E. Blöchl, *Phys. Rev. B* **50**, 17953 (1994).
- [24] G. Kresse and D. Joubert, *Phys. Rev. B* **59**, 1758 (1999).
- [25] G. Kresse and J. Hafner, *Phys. Rev. B* **47**, 558 (1993).
- [26] G. Kresse and J. Furthmüller, *Comput. Mater. Sci.* **6**, 15 (1996).
- [27] G. Kresse and J. Furthmüller, *Phys. Rev. B* **54**, 11169 (1996).
- [28] J. P. Perdew, K. Burke, and M. Ernzerhof, *Phys. Rev. Lett.* **77**, 3865 (1996).
- [29] A. A. Mostofi, J. R. Yates, G. Pizzi, Y.-S. Lee, I. Souza, D. Vanderbilt, and N. Marzari, *Comput. Phys. Commun.* **185**, 2309 (2014).
- [30] N. Marzari, A. A. Mostofi, J. R. Yates, I. Souza, and D. Vanderbilt, *Rev. Mod. Phys.* **84**, 1419 (2012).
- [31] L. Forró, K. Biljaković, J. R. Cooper, and K. Bechgaard, *Phys. Rev. B* **29**, 2839 (1984).
- [32] Z. Zhu, A. Collaudin, B. Fauqué, W. Kang, and K. Behnia, *Nat. Phys.* **8**, 89 (2012).
- [33] A. Collaudin, B. Fauqué, Y. Fuseya, W. Kang, and K. Behnia, *Phys. Rev. X* **5**, 021022 (2015).
- [34] G. Xu, Z. Hou, Y. Wang, X. Zhang, H. Zhang, E. Liu, X. Xi, F. Xu, G. Wu, X.-X. Zhang *et al.*, *J. Phys.: Condens. Matter* **29**, 195501 (2017).
- [35] D. Shoenberg, *Magnetic Oscillations in Metals* (Cambridge University Press, Cambridge, England, 2009).